JBIC (2000) 5 : 236–250

ORIGINAL ARTICLE

Ursula Rothlisberger · Paolo Carloni · Karel Doclo
Michele Parrinello

A comparative study of galactose oxidase and active site analogs based on QM/MM Car-Parrinello simulations

Received 14 October 1999 · Accepted: 19 January 2000

Abstract A parallel study of the radical copper enzyme galactose oxidase (GOase) and a low molecular weight analog of the active site was performed with dynamical density functional and mixed quantum-classical calculations. This combined approach enables a direct comparison of the properties of the biomimetic and the natural systems throughout the course of the catalytic reaction. In both cases, five essential forms of the catalytic cycle have been investigated: the resting state in its semi-reduced (catalytically inactive) and its oxidized (catalytically active) form, $\mathbf{A}^{semi}$ and $\mathbf{A}^{ox}$, respectively; a protonated intermediate **B**; the transition state for the rate-determining hydrogen abstraction step **C**, and its product **D**. For **A** and **B** the electronic properties of the biomimetic compound are qualitatively very similar to the ones of the natural target. However, in agreement with the experimentally observed difference in catalytic activity, the calculated activation energy for the hydrogen abstraction step is distinctly lower for GOase (16 kcal/mol) than for the mimetic compound (21 kcal/mol). The enzymatic transition state is stabilized by a delocalization of the unpaired spin density over the sulfur-modified equatorial tyrosine Tyr272, an effect that for geometric reasons is essentially absent in the biomimetic compound. Further differences between the mimic and its natural target concern the structure of the product of the abstraction step, which is characterized by a weakly coordinated aldehyde complex for the latter and a tightly bound linear complex for the former.

Key words Galactose oxidase · Density functional calculations · Quantum classical calculations · Copper enzymes · Car-Parrinello simulations · QM/MM simulations

U. Rothlisberger (✉) · K. Doclo
Laboratory of Inorganic Chemistry, ETH Zurich, 8092 Zurich, Switzerland
Tel.: +41-1-6327460
Fax: +41-1-6321090
e-mail: uro@inorg.chem.ethz.ch

P. Carloni
International School for Advanced Studies, 34014 Trieste, Italy

M. Parrinello
Max-Planck Institut für Festkörperforschung, Heisenbergstrasse 1, 70569 Stuttgart, Germany

P. Carloni
Istituto Nazionale per la Fisica della Materia (INFM) and International Centre for Genetic Engineering and Biotechnology, 34012 Trieste, Italy

Introduction

The fungal enzyme galactose oxidase (GOase, EC 1.1.3.9) (M_r = 68 kDa, 639 amino acids) catalyzes the stereospecific oxidation of a broad range of primary alcohols to the corresponding aldehydes coupled to the reduction of molecular oxygen to hydrogen peroxide (for reviews on GOase, see e.g. [1–3]). The enzyme contains a single redox active copper ion to carry out this two-electron oxidation reaction. The second redox center was eventually identified as a copper-coordinated, chemically modified tyrosyl radical [4–7]. GOase is thus a member of the increasingly important class of enzymes bearing amino acid based radicals, such as glyoxal oxidase [8], ribonucleotide reductases [9], cytochrome *c* peroxidase [10], prostaglandin H-synthase [11], the oxygen evolving complex of photosystem II [12], and several B_{12} enzymes [13, 14].

The crystal structure of GOase solved in 1991 [15, 16] revealed the active site copper ion to be coordinated in a nearly square pyramidal geometry (Fig. 1a). Two histidine (His496 and His581), one tyrosinate (Tyr272), and a weakly coordinated water molecule (pH 7) or an acetate ion (pH 4.5) occupy equatorial positions. A fifth tyrosinate ligand (Tyr495) is involved in an elongated axial bond ($d_{Cu\text{-}O}$ = 2.6 Å). A peculiar structural feature is the unusual covalent

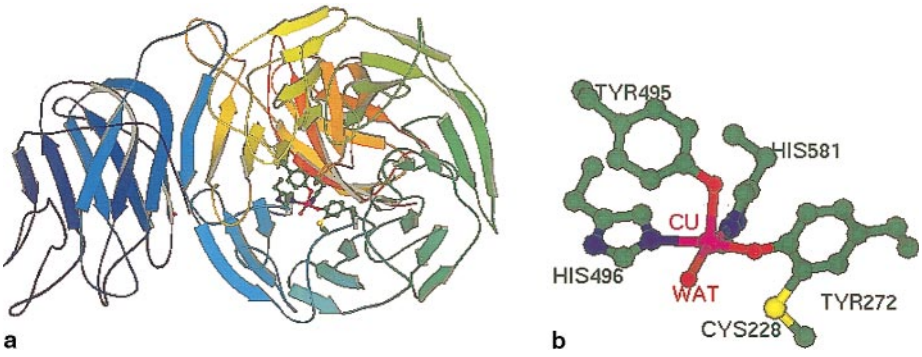

Fig. 1a,b Representation of the secondary structure of the enzyme galactose oxidase [15]; the QM part is indicated in a *ball-and-stick model*

thioether link between the basal Tyr272 and a nearby cysteine (Cys228) (Fig. 1b). It is this *ortho*-modified tyrosine residue that hosts the second redox center of the enzyme [6, 7]. Mutants with an unsubstituted Tyr272 show a substantially lower catalytic activity, indicating that the covalent sulfur link plays an essential role in stabilizing the tyrosyl radical and determining the particular redox properties of the system [17].

GOase can be prepared in distinct semi-reduced (inactive) and oxidized (active) forms [20, 21]. The semi-reduced form is EPR-active and has been identified with the copper(II)-tyrosinate complex shown in Fig. 2 ($\mathbf{A}^{semi}$), whereas the oxidized EPR-silent form was established as an antiferromagnetically coupled copper(II)-tyrosyl species ($\mathbf{A}^{ox}$ in Fig. 2).

A fairly clear picture of the catalytic cycle has emerged during recent years. The proposed reaction mechanism [1–3, 20–22] (Fig. 2) consists formally of two half-reactions, one in which the enzyme is reduced and one in which it is reoxidized [20, 21]. During these two half-cycles the substrate and molecular oxygen are most probably processed successively following a ping-pong mechanism [20]. Starting from the active form of the resting state $\mathbf{A}^{ox}$, the first step of the catalytic cycle involves the binding of the substrate in the basal site adjacent to Tyr272. Substrate binding is followed by a proton transfer in which the axial tyrosinate acts as a general base. Acidified through the coordination of the copper(II) ion, the hydroxyl proton of the alcohol can be transferred to the apical tyrosine Tyr495 [21, 23–25]. Simultaneously, the substrate changes its coordination from a weakly bound complex to a firmly coordinated alcoholate ligand (structure **B** in Fig. 2). Subsequently, a hydrogen atom of the alcoholate is abstracted stereospecifically by the tyrosyl radical site at Tyr272 and an electron is transferred from the resulting ketyl species to the Cu(II) ion, reducing it to Cu(I). Large kinetic isotope effects suggest that the H-abstraction (**C** in Fig. 2) is rate determining under physiological conditions. The exact nature of the corresponding transition state has not yet been identified, and both stepwise [26] and concerted mechanisms [25, 27] have been proposed for the hydrogen and electron transfer processes. After release of the aldehyde, molecular oxygen can bind to the active site and the resting state of the enzyme is regained through the oxidation half-cycle.

The wide range of processed substrates (from propanediol to polysaccharides) and the strict regio- and stereoselectivity [21] render this system of considerable interest for bioanalytical [28] and synthetic applications. Not surprisingly, quite a few biomimetic model compounds have been designed for GOase [26, 29–42]. In spite of a high similarity of structural and/or magnetic properties, most of these synthetic analogs show no catalytic activity. Very recently, however, two groups have succeeded in synthesizing functional models of GOase [40–42]. These new biomimetic compounds catalyze a novel synthetic route for the conversion of primary alcohols to aldehydes and they also constitute well-defined model systems for an investigation of the underlying reaction mechanism.

We have recently performed dynamical density functional calculations of the biomimetic model compounds developed by Stack and co-workers [40]. Our previous study [43] showed that, for the resting state of the synthetic analog, the electronic features are indeed in good agreement with what has been proposed for the natural system. However, in spite of an apparent high structural and electronic fidelity, the synthetic models exhibit a reactivity that is several orders of magnitude below that of GOase. This drastic difference calls for an approach that would allow identification of the essential factors governing the enzymatic reaction that are still missing in the mimetic system.

Here, we report a parallel theoretical study of the enzyme and its synthetic analog aimed at characterization of the main catalytic differences. Several key structures of the catalytic cycle have been investigated in direct comparison with the natural target. To capture the enzymatic system in its full complexity, we have adopted a mixed quantum/classical QM/MM approach in which the active site residues are treated quantum mechanically (within the framework of density functional theory) and the rest of the protein is described with an empirically derived force field. In contrast to pure gas-phase models of the active site, such an approach allows the influence of the protein environment to be assessed and finite temperature

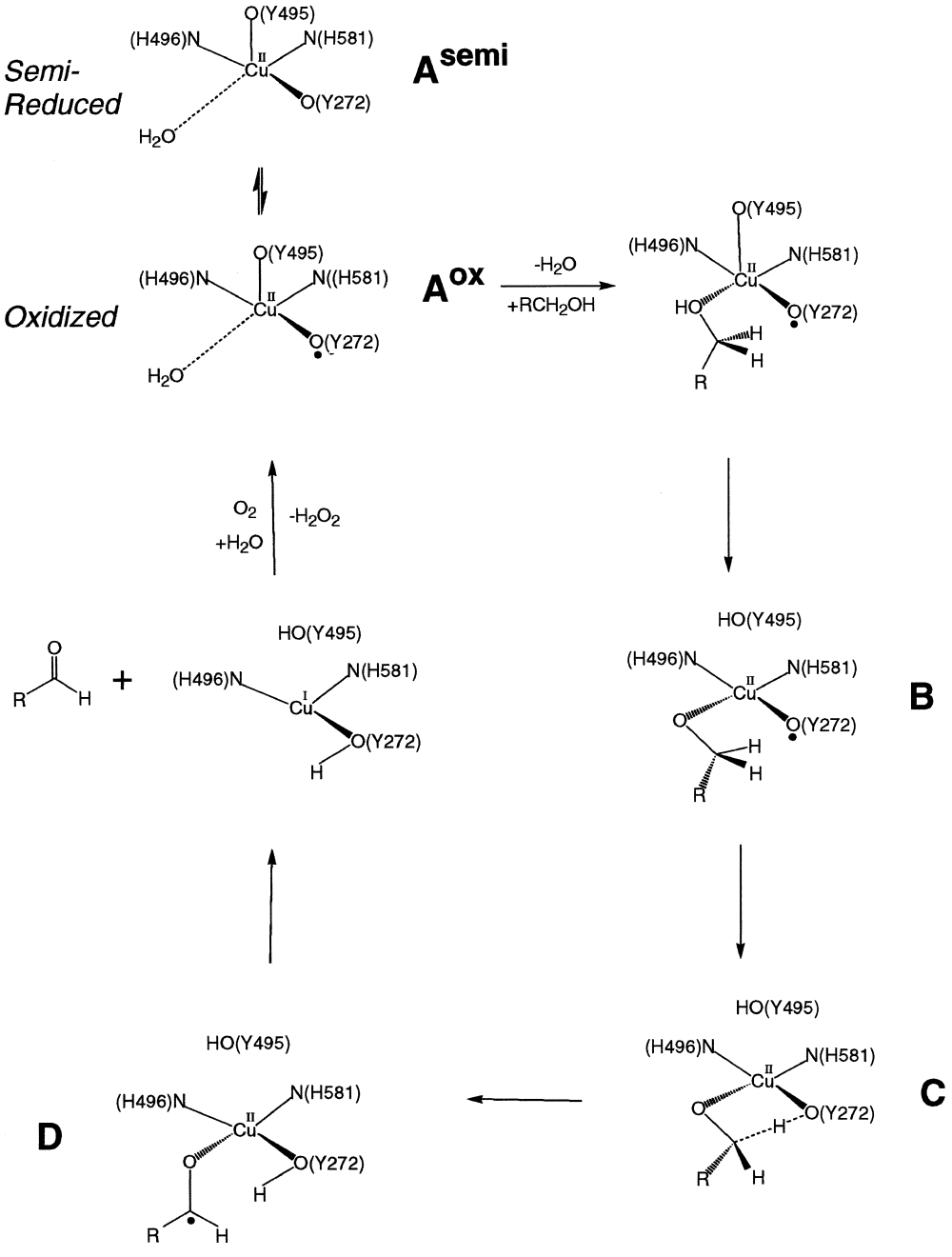

Fig. 2 Schematic representation of the proposed catalytic cycle [1–3]. Labels refer to: ***A*** resting state; ***B*** protonated intermediate; ***C*** transition state of the H-abstraction step; ***D*** product of the abstraction step; *semi* semi-reduced form; *ox* oxidized form

and solvent effects to be captured. In recent years, notable progress has been made in the development of mixed QM/MM simulations techniques and they are becoming an increasingly valuable tool in the study of large complex systems (for a recent review, see [44]). The work we report here is based on a recently developed QM/MM extension of a Car-Parrinello molecular dynamics scheme [45]. In this way, it is possible to perform a comparative study of enzymatic and mimetic systems based on the same theoretical footing. We have compared the two systems for the same catalytic cycle by characterizing the semi-reduced and the oxidized forms of the resting state, $\mathbf{A}^{\text{semi}}$ and $\mathbf{A}^{\text{ox}}$, the protonated intermediate **B**, the transition state for the rate-determining hydrogen abstraction **C,** and the final product of the abstraction step **D**.

Anticipating our results, we find that in both forms of the resting state the electronic structures of the natural and synthetic systems are remarkably similar. For both, the unpaired electron of the semi-reduced form $\mathbf{A}^{\text{semi}}$ is located in a $d_{x^2-y^2}$ orbital of the copper, whereas the catalytically active oxidized form $\mathbf{A}^{\text{ox}}$ is characterized by an antiferromagnetically coupled diradical state. Notably, the second unpaired electron is located on the *axial* tyrosinate ligand in both sys-

tems. We have also observed no major qualitative differences for the protonated intermediate **B**. Upon protonation of the apical ligand, the second unpaired electron transfers to the *equatorial* tyrosinate (Tyr272 in GOase), with additional delocalization over the covalently linked sulfur atom. More distinct differences exist for **C** and **D**. The transition state for the hydrogen abstraction is significantly higher in the mimetic system (21 kcal/mol) than in the enzyme (16 kcal/mol). In the biological system, the radical state is additionally stabilized by a delocalization over the equatorial Tyr272 and the covalent sulfur link to Cys228. For geometric reasons, this delocalization is not effective in the biomimetic compound. Furthermore, as a consequence of the particular nature of the biomimetic ligand system, the energetically most favorable synthetic product structure differs clearly from the one obtained for the natural system.

Materials and methods

Static and dynamic [46] density functional calculations [47, 48] were performed with the CPMD program [49]. In this code, systems are treated within periodic boundary conditions and a basis set of plane waves. For all our present calculations the one-particle orbitals of the valence electrons have been expanded up to a kinetic energy cutoff of 80 Ry. To represent the effect of the core electrons we used soft normconserving pseudo-potentials of the Troullier-Martins type [50]. All the calculations were done with the gradient-corrected exchange-correlation functionals developed by Becke [51] and by Lee, Yang, and Parr [52] (BLYP). Charged systems were treated with a method developed by Hockney [53, 54]. The same approach was adopted to isolate the long-range Coulomb interactions of the quantum part from its (classical) environment. Examples of the performance of our computational scheme have been given previously [43].

Static and dynamic density functional calculations of the biomimetic system

The starting point of our calculations on the synthetic analog was the crystal structure [40] of one of the biomimetic compounds (Fig. 3b) in its semi-reduced resting state ($\mathbf{A}^{semi}$). In our previous study, we used this system as a test case to validate the performance of our computational scheme [43]. We demonstrated that extensive geometry optimization of the entire 105 atoms comprising open-shell system reproduced the experimental structure very closely. In the same study [43] we determined the lowest energy structure of the oxidized form ($\mathbf{A}^{ox}$) in a complex with the substrate analog methoxide (MeO^-), for which EXAFS data are available [40]. Our previous work thus confirmed the applicability and accuracy of our theoretical scheme. Therefore, the same computational approach was adopted in the current study. The forms **B – D** of the catalytic cycle were optimized through a combined approach in which electronic and geometric degrees of freedom were relaxed simultaneously (the treatment of open-shell singlet states requires special care and is described in the last paragraph of this section). Starting from the equilibrium geometry of $\mathbf{A}^{ox}$, we generated the protonated form **B** and performed a first preoptimization of the structure using the molecular modeling package CERIUS2 [55]. The geometry of the protonated oxygen ligand was first relaxed with force-field-based energy minimization, with the rest of the complex kept at a fixed geometry. The Dreiding 2.1 force field [56] with charge equilibration [57] derived atomic point charges was used for this purpose. The initial geometry generated in this way was subjected to a full structural and electronic optimization at the gradient-corrected density functional level. The transition state of the hydrogen abstraction step (**C**) was located by performing molecular dynamics runs at low temperature in which the hydrogen-oxygen distance involved in the transfer was constrained at different values while the rest of the complex was allowed to relax freely. The transition state (**C**) was located by the change of sign of the constraint force. The distance constraint was released from a configuration with a 0.1 Å smaller H-O distance than in the transition state. A subsequent geometry optimization with dynamic and local optimization techniques led to the product (**D**). We employed face-centered cubic supercells of edges $a = 26.5$ Å and 23.0 Å for the neutral systems $\mathbf{A}^{semi}$ and $\mathbf{A}^{ox}$, respectively. The monocharged systems **B–D** were calculated in orthorhombic supercells with $a = 16.2$, $b = 16.3$, and $c = 16.5$ Å using the electrostatic decoupling scheme developed by Hockney [53, 54].

QM/MM simulations of galactose oxidase

The enzymatic system was treated within a combined quantum/classical (QM/MM) approach [45]. The same theoretical scheme as described above for the biomimetic system was used to describe the quantum region (QM). This part of the system (shown in Fig. 3a) consisted of ~70 atoms including the copper ion and its four direct ligands His496, His581, Tyr272, and Tyr495. The fifth ligand was either water (in $\mathbf{A}^{semi}$ and $\mathbf{A}^{ox}$) or a methanol substrate in its various processed forms during the catalytic cycle **B–D**. For all the calculations the covalently linked cysteine residue Cys228 as well as a varying number of active-site water molecules (2–6) were also treated quantum mechanically. The surrounding protein was described with the classical molecular dynamics package EGO VIII [58]. EGO is based on the CHARMM force field [59] and one of its particular features is the fact that long-range Coulomb forces are described with a hierarchical multipole algorithm [60], thus enabling the treatment of large systems. The classical part (MM) in our study consisted of a total of about 16,000 atoms (~7000 protein atoms and ~3000 water molecules). We have only included the protein domains D2 and D3 [16], while D1 was left out in our simulations. This simplification seems to be justified as D1 (155 amino acids) is located far from the active site and is thought to have no direct influence on the catalytic activity [16].

In mixed quantum/classical simulations, special care has to be taken in the choice of the atoms at the QM/MM interface. For the case where the border between QM and MM part runs across a covalent bond, the QM part has to be saturated to retain a closed-shell system. We have chosen our QM model in such a way that only relatively nonpolar carbon-carbon bonds are cut. The last atoms of the QM part (the β-carbon of His496 and His581, and the α-carbon of Tyr272, Tyr495, and Cys228)

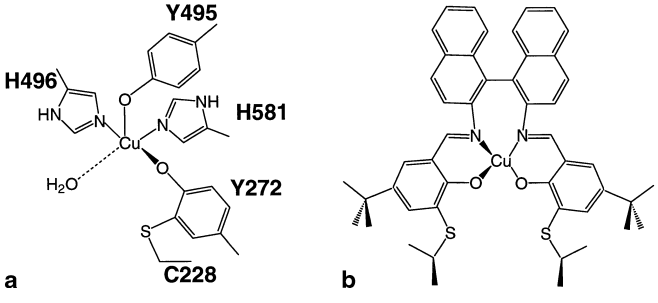

Fig. 3 **a** Schematic representation of the active site of galactose oxidase (GOase) in comparison with **b** the biomimetic model compound [40]

were replaced by hydrogen and treated with the scaled position method for link atoms (SPLAM) [45].

The following protocol was applied for the determination of the different forms **A–D** of the catalytic cycle. Two crystal structures, one at neutral and one at low pH (7.0 and 4.5), have been determined for GOase [16]. Only minor differences exist between the two structures [16] and we therefore opted for the low pH form with a somewhat higher resolution (1.7 Å versus 1.9 Å for the high pH form) as our initial structural model. Missing hydrogens were added, assuming standard bond lengths and angles. Protons were added according to a pH of 7. The protein was surrounded with a shell of water molecules with a thickness of 4 Å. The resulting system was minimized with the molecular dynamics package X-PLOR [61]. Heavy atoms were kept fixed at their original positions in the crystal and hydrogen atoms were relaxed with molecular dynamics runs. The resulting configuration served as input for the mixed QM/MM simulations of the forms **A–D** of the catalytic cycle. For each form, the structure was first kept frozen and only the initial electronic wavefunction was optimized using low-temperature molecular dynamics runs of the electronic degrees of freedom (see next paragraph). Then the electronic and geometric structures of the QM part were allowed to relax simultaneously under the influence of the external potential from the surrounding MM part. During this first relaxation the classical part was kept frozen in one single configuration until the QM part was equilibrated. Subsequently, the full system (QM and MM parts) was allowed to move. In the MM part, bonds involving hydrogens were kept at a fixed value with SHAKE [62] while no constraints were imposed on the QM part. The system was cooled down by rescaling the ionic velocities with a factor of 0.9–0.95 at every time step of 1–2 fs. After 0.5–2 ps the systems reached stable minimum configurations with converged values of the QM energy. For all the different forms **A–D** the final temperature of the system was below 1 K. Naturally, in a complex fluctuating medium such as a protein in solution one expects the system to visit several configurations [63]. However, we consider the resulting equilibrium structures as typical examples for the ensemble of thermally accessible configurations. This approach allowed us to compare relative energies of different systems without having to resort to full free-energy calculations which would be prohibitive even for state-of-the-art computer power. We also investigated finite temperature effects by performing a simulation of $\mathbf{A}^{ox}$ at 310 K. The resulting influence on the distribution of the unpaired spin density of the catalytically active diradical state is minor.

The transition state **C** for the hydrogen abstraction step was determined by applying systematically varied restraints on the corresponding H-O distance. The applied force constant was 10 au.

Optimization of the electronic structure

In the catalytically active species we are concerned with an antiferromagnetically coupled diradical state. For such an open-shell singlet state, several electronic minima can exist, including states with completely paired or only weakly coupled valence electrons. Depending on the number of energetically competitive one-electron levels, the electronic problem can be complex. Instead of performing several different calculations for each electronic configuration (with, for instance, different initial occupations of the one-electron levels), we adopt here a combined approach in which a single calculation is performed to find the energetically most favorable electronic minimum. Consistent with a Car-Parrinello approach [46], we perform molecular dynamics simulated annealing runs at low temperature for the (fictitious) electronic degrees of freedom. In this way, small barriers between different electronic states can be overcome thermally. Whereas standard methods with local optimization techniques only converge to the nearest electronic minimum, the dynamic scheme is able to accomplish a more global optimization. All our calculations were initiated with a completely paired state with no net spin polarization and the dynamical optimization led invariably to the antiferromagnetically coupled state. Closed-shell singlet states are only a few kcal/mol higher in energy. Furthermore, in a similar way, a simultaneous optimization of electronic and geometric degrees of freedom can be performed. This proved to be advantageous because of a strong coupling between the specific nature of the electronic state and the geometric properties (e.g. the ligand binding at the copper ion). Once geometric and electronic structure had converged to stable values, we used also local relaxation techniques such as steepest descent and preconditioned conjugate gradient with line search for a final optimization.

Results and discussion

In the following sections we present a detailed comparison of the structural and electronic properties of the enzymatic system and its mimic in the different forms **A–D** of the catalytic cycle.

Resting state **A**

In its resting state, GOase consists of a mixture of a catalytically inactive (semi) reduced form $\mathbf{A}^{semi}$ and the actual active oxidized species $\mathbf{A}^{ox}$. Both forms have also been observed for the mimetic compound. Furthermore, the natural and synthetic systems exhibit also the same magnetic properties, namely an EPR-active and an EPR-silent form for $\mathbf{A}^{semi}$ and $\mathbf{A}^{ox}$, respectively. We have performed calculations of the former in a doublet and of the latter in an open-shell singlet state.

Structural properties

In Table 1 we compare characteristic structural features of $\mathbf{A}^{semi}$ and $\mathbf{A}^{ox}$ for the natural system and its mimic. Crystallographic data have also been included where available. The low-temperature configuration that we obtained from our equilibrated and annealed solution structure of GOase is in good agreement with the crystal structures at low and at neutral pH. For the quantum region, the root mean square (RMS) deviation between calculated and experimental values augments to only 0.1 Å/atom. Characteristic structural parameters of the copper coordination polyhedron are compared in detail in Table 1. The copper-oxygen bonds to the two coordinated tyrosine residues are reproduced within a few hundreds of an angstrom. The third Cu-O distance refers to an acetate ion in the crystal structure at pH 4.5 (with a short Cu-O distance $d_{Cu\text{-}O}$ of 2.26 Å) and to an only loosely coordinated water molecule ($d_{Cu\text{-}O} = 2.8\text{–}3.0$ Å) in all the other structures. In view of the weak nature of the coordination bond to H_2O, the discrepancy of about 0.1–0.2 Å between calculated and experimental geometries seems easily explainable. The calculated Cu-N

Table 1 Characteristic structural properties of the copper coordination polyhedra for the resting states $\mathbf{A}^{semi}$ and $\mathbf{A}^{ox}$ of the natural system (GOase) and its synthetic analog (Mimetic). Corresponding experimental results from X-ray studies are also included[a,b]

	Mimetic X-ray $\mathbf{A}^{semi}$	Mimetic $\mathbf{A}^{semi}$	Mimetic $\mathbf{A}^{ox}$	GOase $\mathbf{A}^{semi}$	GOase $\mathbf{A}^{ox}$	GOase X-ray-4.5	GOase X-ray-7.0
$d_{Cu\text{-}O1}$	1.89	1.91	2.39	2.62	2.60	2.69	2.59
$d_{Cu\text{-}O2}$	1.90	1.92	1.92	1.90	1.86	1.93	1.91
$d_{Cu\text{-}O}$	–	–	1.89	2.99	2.95	2.26	2.81
$d_{Cu\text{-}N1}$	1.98	1.95	2.02	1.95	1.94	2.11	2.24
$d_{Cu\text{-}N2}$	1.96	1.95	1.97	2.24	2.20	2.14	2.21
$\angle$ O1CuO2	87	91	117	83	83	75	79
$\angle$ O1CuO	–	–	87	90	92	91	87
$\angle$ O1CuN1	93	94	80	98	96	106	102
$\angle$ O1CuN2	157	144	93	105	105	97	106
$\angle$ O2CuO	–	–	90	74	74	83	76
$\angle$ O2CuN1	158	146	161	163	162	172	169
$\angle$ O2CuN2	92	95	93	106	106	99	100
$\angle$ OCuN1	–	–	84	89	89	90	93
$\angle$ OCuN2	–	–	175	163	165	172	166
$\angle$ N1CuN2	96	100	92	90	91	89	91
$\angle \phi_1$	31	45	88	75	75	83	73

[a] X-ray $\mathbf{A}^{semi}$ refers to the crystal structure of the mimetic compound [40]; X-ray-4.5 and X-ray-7.0 refer to the enzymatic system at low and at neutral pH [16]. The labels $d_{Cu\text{-}X}$ and $\angle$ XCuY refer to bond distances (Å) and bond angles (°)

[b] The following atomic labeling scheme has been used: O1, oxygen atom of the axial ligand (Tyr495 in GOase); O2, oxygen atom of the equatorial ligand (Tyr272 in GOase); N1, nitrogen atom in *trans* position to O2 (Nε2 of His496 in GOase); N2, nitrogen atom in *trans* position to the substrate (Nε2 of His581 in GOase); O, oxygen atom at the substrate binding site (H_2O, acetate, or methoxide). $\angle \phi_1$ refers to the angle between the planes spanned by the atoms O1CuN1 and O2CuN2

distances to the two histidine residues are slightly underestimated (1.95–2.25 Å compared with 2.11–2.24 Å in the crystal structures). From a short (0.9 ps) molecular dynamics run around 310 K it becomes apparent that these distances can undergo rather large thermal fluctuations (1.7–2.4 Å) on a short time scale. A first indication of the variability of these bonds can also be drawn from the comparison of the two crystal structures, which give values that differ by as much as 0.1 Å. We observe also sizeable thermal fluctuations for the Cu-O distance to the axial tyrosine Tyr495 which can vary over a range of 1.8–4.1 Å. All bond angles involving the copper ion are reproduced to within 1–6°. The agreement is especially striking for the angle ϕ_1 between the plane spanned by the His496-N, the copper ion, and the Tyr495-O and the one defined by the His581-N, the copper ion, and the Tyr272-O. This angle, which serves as a measure for the distortion of the copper coordination polyhedron between a tetrahedral and a square pyramidal geometry, is reproduced to within 2°. Only very small differences exist between the calculated active-site geometries for $\mathbf{A}^{semi}$ and $\mathbf{A}^{ox}$. Upon oxidation, bond lengths are slightly shortened (by less than 0.04 Å) and bond angles remain the same within 2°. These findings are in agreement with experimental data from EXAFS studies that indicate no major structural changes between the semi-reduced and the oxidized form [64].

Corresponding structural parameters of the biomimetic compound are also summarized in Table 1. A comparison of the optimized geometry for $\mathbf{A}^{semi}$ with the experimental X-ray structure reconfirms the adequacy of our computational scheme. All the coordination bonds to copper are reproduced within 0.03 Å and angles are generally within 1–4° (some larger deviations of up to ~10° exist for two specific angles which are most likely caused by the absence of crystal packing effects [43]).

For the reduced form of the resting state, quite prominent structural differences exist between the synthetic model and its natural target. With a distortion angle ϕ_1 (as defined above) of 45°, the biomimetic compound assumes a geometry around the copper ion that cannot be described by any idealized coordination polyhedron. GOase instead forms a slightly distorted square pyramidal geometry with $\phi_1 = 75°$. The two Cu-O and Cu-N bonds are of similar length (1.91–1.95 Å) in the synthetic compound, while for the natural system the axial ligand distance is clearly elongated (2.6 Å). However, as the semi-reduced form $\mathbf{A}^{semi}$ is not directly involved in the catalytic reaction, these differences are unlikely to bear a direct consequence on the catalytic activity itself. Upon oxidation and substrate binding, rather drastic geometric (and electronic) changes occur that render the structure of the catalytically relevant oxidized form $\mathbf{A}^{ox}$ of the biomimetic much closer to the one of its natural counterpart. The binding of the substrate analog methoxide in the equatorial plane of $\mathbf{A}^{semi}$ completes a square pyramidal coordination geometry with $\phi_1 = 88°$ and an elongated axial Cu-O bond that is only slightly smaller (2.4 versus 2.6 Å) than in the enzymatic system, where the long axial ligand distance is additionally stabilized by the protein environment. For steric reasons, the alkyl residue on the sulfur

atom of the equatorial ligand (that mimics the covalent link to Cys228) has to be displaced significantly to accommodate the substrate. In $\mathbf{A}^{semi}$, one of the axial alkyl groups assumes an in-plane conformation whereas the equatorial one forms an angle of 53° with respect to the plane of the aromatic ring system. In the methoxide complex of $\mathbf{A}^{ox}$ this second group is turned away from the substrate in such a way that the C-S bond is rotated by 127° into an in-plane configuration (Figs. 4b and 5b). These rather drastic structural rearrangements involving the change of the copper coordination geometry, a shift of the axial ligand, and a rotation of the equatorial thioether group should be contrasted with the essentially unchanged geometries of $\mathbf{A}^{semi}$ and $\mathbf{A}^{ox}$ in the natural system. Some differences between the mimetic and the natural compounds exist also in the orientation of the aromatic ligands. For instance, the ring of the aromatic system of the equatorial oxygen ligand is oriented coplanar with respect to the equatorial CuO_2N_2 plane, whereas the corresponding aromatic ring of Tyr272 is almost perpendicular (77°) to the equatorial plane. Further differences exist concerning solvation in the two systems. Experimentally, the catalytic reaction of the synthetic compound is most efficiently performed in solutions of the substrate itself and we have not included any additional solvent molecules in our gas phase model. In the active site of the enzyme, on the other hand, several water molecules are present. One of them forms a hydrogen bond to the oxygen atom of Tyr272 in the low-temperature configurations of the resting state **A**. Overall, however, the geometry of $\mathbf{A}^{ox}$ resembles quite closely the structure of the active site, which is also demonstrated by the fairly good agreement of the coordination bond angles of the mimetic and the natural systems (Table 1).

Electronic structure

The main electronic features of the mimetic and the natural systems are remarkably similar for the resting state. Figures 4 and 5 show comparisons of the distribution of the unpaired spin density for the semi-reduced and the oxidized forms. In agreement with the proposed catalytic mechanism [1–3] and experimental EPR data [7], the single unpaired electron is localized on the Cu(II) ion in $\mathbf{A}^{semi}$. For both the enzymatic (Fig. 4a) and the synthetic (Fig. 4b) systems the unpaired electron occupies the $d_{x^2-y^2}$ orbital with some additional delocalization over the electron-donor atoms of the direct ligands. For a more quantitative comparison we have integrated the unpaired spin density in a sphere of a radius of 2 au around each atom, except for copper, for which a radius of 4 au was assumed. The number of unpaired electrons per atom obtained in this way is given in Table 2. In spite of some structural differences, the synthetic system is capable of reproducing the electronic properties of GOase quite faithfully. The spin density distribution in the enzymatic system is with ~0.5e on the copper and a further 0.3e on the coordinated electron-donor atoms, more diffuse than in the biomimetic compound for which the corresponding values turn out to be ~0.9e and 0.3e, respectively.

The similarity is even more pronounced for the active forms $\mathbf{A}^{ox}$ (Fig. 5a and b). In both systems, one unpaired electron of α-spin is localized on the copper ion whereas an electron of opposite spin is spread over the *axial* oxygen-containing ligand, consistent with an antiferromagnetically coupled species proposed for $\mathbf{A}^{ox}$ [1–3]. For GOase, integration of the unpaired spin density yields values $\rho_\alpha = 0.75$e on the copper and $\rho_\beta = 0.9$e on the axial tyrosine Tyr495. Corresponding numbers for the mimetic system are in turn $\rho_\alpha = 0.7$e and $\rho_\beta = 0.35$e.

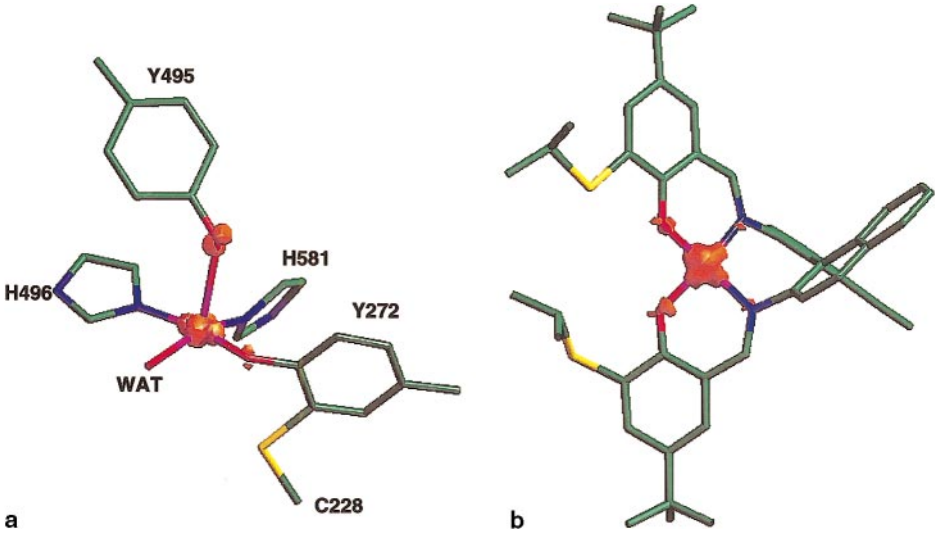

Fig. 4 Contour plots of the unpaired electron density distribution in the semi-reduced form of the resting state of **a** GOase and **b** the biomimetic compound (contour at 0.02e/au^3)

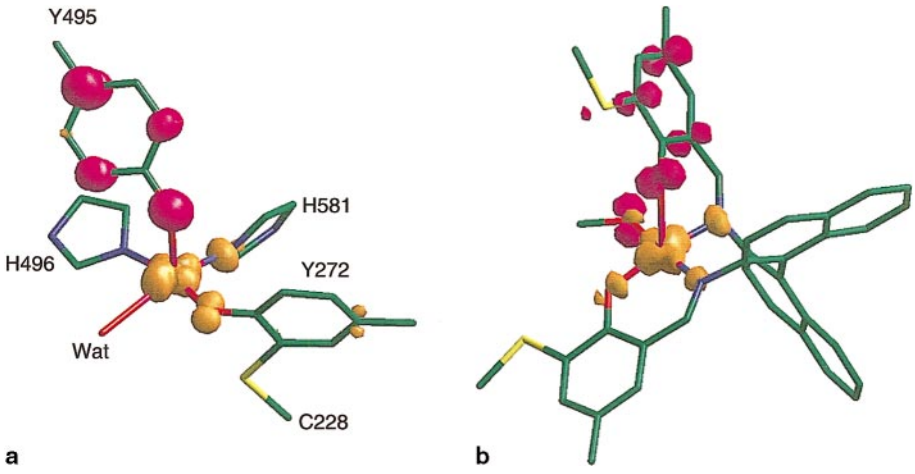

Fig. 5 Contour plots of the unpaired electron density distribution in the oxidized form of the resting state of **a** GOase and **b** the biomimetic compound. Contours are drawn at 0.002e/au^3. *Orange* and *magenta* refer to α- and β-spin densities, respectively

We have performed several computer experiments to identify the main factors that can influence the particular antiferromagnetic spin distribution in the biological system. We noticed that the β-spin distribution is distinctly sensitive to the position of the axial ligand. As mentioned earlier, rather large fluctuations of the axial Cu-O distance can occur. We observed that for shorter Cu-O distances the unpaired β-spin density can delocalize easily also over the equatorial tyrosine. For the short Cu-O distances around $d_{\text{Cu-O}} = 2.1$ Å, we find that about half a β-electron is localized on each of the tyrosine ligands. On average, however, the spin distribution is not affected significantly by thermal effects, as illustrated by the values of a typical finite temperature configuration listed in Table 2 in comparison with the 0 K distribution. We have also tested the effect of the surrounding field of the protein. Keeping the geometry of the quantum part at a fixed value, we have switched off the surrounding field and reoptimized the electronic wavefunction. A plot of the spin distribution difference with and without external field is shown in Fig. 6. The external field of the protein induces a slightly more diffuse distribution by lowering the unpaired spin density at the copper ion and at the oxygen atom of Tyr495. However, the effects of the external field are rather small in the case of $\mathbf{A}^{\text{ox}}$. The relative change in the spin population augments to 0.08e on the copper and to 0.04e on the axial tyrosine ligand.

Protonated intermediate **B**

An important step in the catalytic cycle involves the deprotonation of the copper-coordinated alcohol substrate [26]. Based on spectroscopic measurements,

Table 2 Unpaired spin distributions for the resting state[a] (given in number of electrons)

	Mimetic $\mathbf{A}^{\text{semi}}$	Mimetic $\mathbf{A}^{\text{ox}}$	GOase $\mathbf{A}^{\text{semi}}$	GOase $\mathbf{A}^{\text{ox}}$	GOase $\mathbf{A}_{310}$
Cu	−0.91	−0.55	−0.54	−0.60	−0.56
O1	−0.08	+0.13	−0.17	+0.25	+0.27
1-*ortho*	0.00	+0.08	−0.05	+0.10	+0.15
1-*meta*	0.00	0.01	0.00	−0.02	−0.04
1-*para*	0.00	+0.10	−0.07	+0.16	+0.25
O2	−0.08	−0.05	−0.07	−0.07	−0.12
2-*ortho*	0.00	0.00	−0.03, −0.02	−0.03	−0.07, −0.03
2-*meta*	0.00	0.00	0.00	+0.02	−0.01
2-*para*	0.00	0.00	−0.03	−0.04	−0.065
S	0.00	0.00	0.00	0.00	−0.08
CuL_{tot}	−1.20	−0.82	−0.83	−0.75	−0.75
Ax_{tot}	−0.09	+0.50	−0.22	+0.88	+1.1
Eq_{tot}	−0.09	−0.00	−0.15	−0.17	−0.35

[a] Atom labeling as in Table 1. 1-*ortho*, 1-*meta*, 1-*para* refer to the carbon atoms in *ortho*, *meta*, and *para* positions of the axial oxygen-containing (O1) ligand; 2-*ortho*, 2-*meta*, 2-*para* refer to the ones of the equatorial oxygen-containing (O2) ligand; owing to the asymmetry induced by the sulfur substitution, two values are given if the two *ortho* populations are non-identical; S is the covalently linked sulfur atom on the equatorial ligand (Cys228-S in GOase): CuL_{tot} is the total integrated α-spin density on the copper ion (including the oxygen and nitrogen donor atoms); Ax_{tot} and Eq_{tot} are the total unpaired spin density on the axial and equatorial oxygen ligands (Tyr495 and Tyr272 in GOase)

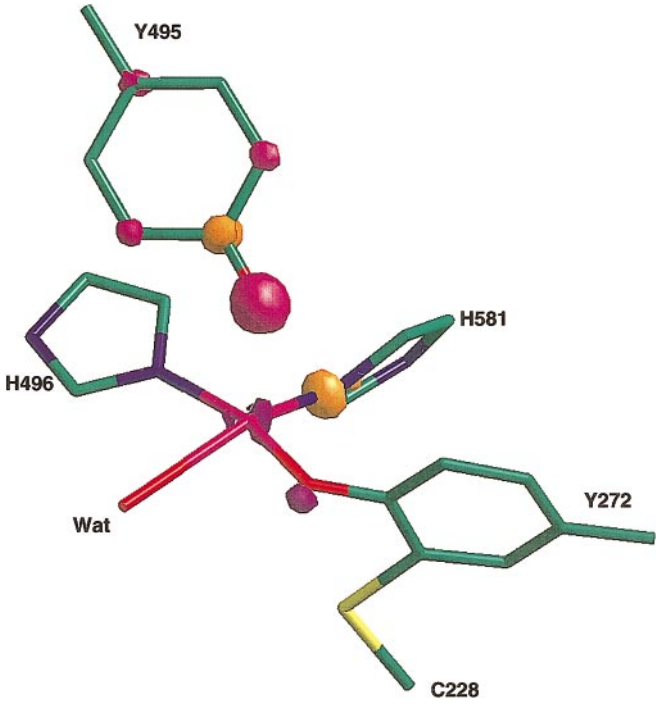

Fig. 6 Environment effect on the unpaired spin distribution in $\mathbf{A}^{ox}$ of GOase. Difference plot of the unpaired spin density distribution with and without external protein field (see text). Contour is shown at $+0.006$e/au^3 (orange) and -0.006e/au^3 (magenta)

Whittaker and Whittaker [23] suggested that the axial tyrosine Tyr495 acts as a base and becomes uncoordinated upon protonation. This interpretation is further supported by site-directed mutagenesis experiments on Tyr495Phe mutants, which show a 1100-fold reduction of k_{cat}/K_M [24]. The proton transfer step is estimated to have a vanishing or very small (~ 1 kcal/mol) energy barrier [22] and clearly does not compete for the rate-determining process. Thus, as the next key structure of the catalytic cycle, we have gone on directly to consider the final product **B** of the protonation step without a detailed mechanistic investigation of its generation from $\mathbf{A}^{ox}$.

Structural properties

Some characteristic structural parameters of the protonated intermediate **B** are summarized in Table 3 for the natural system and its synthetic analog. For both cases, only small structural changes occur with respect to $\mathbf{A}^{ox}$. The main rearrangement concerns the axial ligand, which moves away from the copper ion upon protonation, and a tightening of the copper substrate bond from a $d_{Cu\text{-}O}$ value of 1.90 Å to 1.86 Å. In the synthetic compound a simultaneous rotation of the axial oxygen-containing aromatic ligand takes place in such a way that it becomes almost coplanar with the adjacent nitrogen-containing heterocycle. Thereby, the angle between the two aromatic systems is reduced from 50° in $\mathbf{A}^{ox}$ to 21° in **B**. At the same time, the hydroxyl proton of O1 forms a new intramolecular hydrogen bond to N1. Similarly, in the natural system the hydroxyl proton of Tyr495 is involved in two hydrogen bonds, to Tyr272 (O2) and to the alcohol substrate. Furthermore, Tyr495-O1 is in hydrogen bonded contact with a water molecule.

Electronic structure

As for the resting state, the electronic structure of the protonated intermediate turns out to be rather similar for the natural and the synthetic systems. As in the case of $\mathbf{A}^{ox}$, the electronic structure is characterized by an antiferromagnetically coupled diradical state in

Table 3 Characteristic structural parameters of the protonated intermediate (**B**), the transition state for hydrogen abstraction (**C**), and the product of the abstraction step (**D**)[a]

	Mimetic **B**	Mimetic **C**	Mimetic **D**	GOase **B**	GOase **C**	GOase **D**
$d_{Cu\text{-}O1}$	(3.19)	(3.43)	(3.34)	(2.89)	(2.86)	2.55
$d_{Cu\text{-}O2}$	1.91	1.94	2.38	1.91	1.92	2.31
$d_{Cu\text{-}O}$	1.86	1.96	1.85	1.86	2.00	2.66
$d_{Cu\text{-}N1}$	2.09	2.02	(3.12)	1.99	1.95	1.96
$d_{Cu\text{-}N2}$	1.97	1.96	1.84	2.02	1.91	1.97
∠ O2CuO	90	82	94	85	80	68
∠ O2CuN1	171	164	151	169	164	147
∠ O2CuN2	93	92	90	101	101	112
∠ OCuN1	84	88	79	86	86	80
∠ OCuN2	176	173	176	173	174	168
∠ N1CuN2	94	99	98	87	95	101
$\angle \phi_2$	7	13	24	29	9	12
$d_{C\text{-}O}$	1.42	1.33	1.25	1.43	1.33	1.23
$d_{C\text{-}H}$	1.10	1.39	(4.20)	1.11	1.38	(2.58)
$d_{H\text{-}O2}$	(2.46)	1.25	1.00	2.23	1.24	0.98
∠ HCH	108	117	119	108	115	117

[a] Atom labeling as in Table 1; ϕ_2 refers to the angle between the planes spanned by the atoms N1CuO and O2CuN2; C and H refer to carbon and hydrogen atoms of the substrate; the H in $d_{H\text{-}O2}$ refers to the hydrogen atom of the substrate nearest to O2

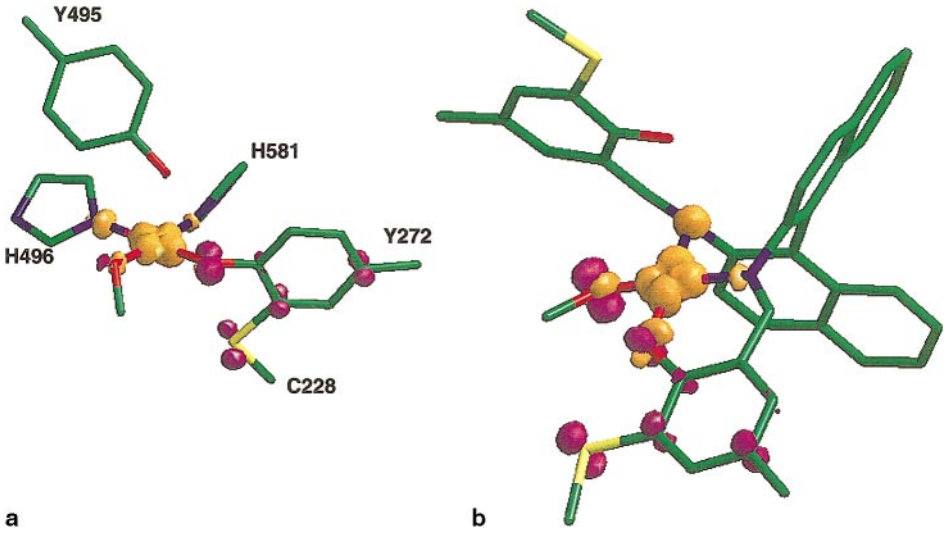

Fig. 7 Comparison of the unpaired electron density distribution of the protonated intermediate **B** of **a** GOase and **b** the biomimetic compound (contour at 0.008e/au^3). *Orange* and *magenta* refer to α- and β-spin densities, respectively

which one unpaired electron is mainly localized on the Cu(II) ion. The second unpaired electron, however, switches position from the *axial* to the *equatorial* tyrosine upon protonation at O1 (Fig. 7a and b). In agreement with the role suggested for Cys228 in GOase [1–3], the radical state is additionally stabilized through delocalization over the covalently linked sulfur atom. The effect of the sulfur substitution is also clearly apparent in the induced asymmetry of the unpaired electron distribution of the aromatic system (as signaled by the difference in spin population of the two *ortho*-carbon atoms). A quantitative comparison of the unpaired spin distribution (Table 4) shows that 0.07 unpaired β-electrons are localized on the equatorial sulfur atom in GOase and 0.09 in the synthetic compound. The total integrated spin density on the equatorial ligand adds up to 0.4e for both systems, whereas less than 0.06 unpaired electrons remain on the axial one. As for the resting state, the unpaired α-spin density at the copper is slightly more diffuse in GOase (0.6e) than in the mimic (0.8e). A discrepancy between the natural and the synthetic systems is caused by the difference in the orientation of the sulfur-substituted equatorial ligand. In GOase, the aromatic plane of Tyr272 is almost perpendicular (~ 77°) to the CuO_2N_2 plane, while the corresponding ligand in the mimetic system is coplanar. As a consequence, the p_z orbitals of Tyr272 hosting the unpaired β-electron are essentially parallel to the $d_{x^2-y^2}$ orbital of the copper bearing the unpaired α-electron. This is in contrast to the situation in the synthetic analog, where the corresponding orbitals are mutually orthogonal[1]. For the mimetic compound, the only β-orbitals with some overlap to α-orbitals are located on the substrate which carries also a distinctly higher unpaired spin density (0.13e) than in the natural system (0.03e).

Table 4 Unpaired spin distributions in the protonated intermediate (**B**) and in the transition state for hydrogen abstraction (**C**)[a]

	Mimetic **B**	Mimetic **C**	GOase **B**	GOase **C**
Cu	−0.61	−0.51	−0.47	−0.50
O2	−0.05, +0.07	+0.06, −0.01	−0.01, +0.07	−0.01, +0.09
2-*ortho*	+0.03, +0.05	–	+0.03, +0.06	+0.01
2-*meta*	–	–	−0.02, +0.02	−0.01
2-*para*	+0.07	–	+0.06	+0.02
S	+0.09	–	+0.07	+0.01
O	−0.04, +0.11	+0.17	−0.03, +0.02	−0.02, +0.12
C	+0.01	+0.22	+0.01	+0.21
H	+0.01	+0.19	+0.01	+0.16
CuL_{tot}	−0.80	−0.62	−0.60	−0.63
Eq_{tot}	+0.41	+0.075	+0.36	+0.13
Sub_{tot}	+0.13	+0.69	+0.03	+0.63

[a] Atom labeling as in Tables 2 and 3

Transition state of the hydrogen abstraction step **C**

The stereoselective abstraction of a hydrogen atom from the deprotonated substrate to the oxygen atom of Tyr272 has been suggested as partially, or most likely, the main rate-determining step in the catalytic reaction of GOase [20]. This conclusion is supported by the large kinetic isotope effect (KIE) of ~ 22 which results upon deuteration of the alcohol substrate [20]. A similar effect, even though less pronounced (KIE ~ 5 [40]), has also been observed for the mimetic system.

[1] A decrease in overlap between α- and β-orbitals can lead to an enhanced stability of the triplet state. We have calculated the singlet/triplet separation for $\mathbf{A}^{ox}$ of the mimetic compound. In $\mathbf{A}^{ox}$ the second unpaired electron is located at the axial ligand for which the p_z ring orbitals have a coplanar orientation with the $d_{x^2-y^2}$ at the copper, thus favoring the singlet state by 1.5 kcal/mol (~ 500 cm^{-1}). A subsequent conversion to the triplet state is spin forbidden and we have therefore performed all the calculations of the catalytic reaction for the (open-shell or closed-shell) singlet state

We have determined the transition state **C** for the hydrogen abstraction for both the natural and the synthetic systems as described in Materials and methods.

Structural properties of **C**

Characteristic structural parameters for the transition state **C** are listed in Table 3 in comparison with the corresponding data for the initial (**B**) and the final states (**D**) of the hydrogen abstraction step. Only minute geometric changes take place with respect to the protonated intermediate **B**. For both the synthetic and the natural systems the RMS between **B** and **C** is less than 0.005 Å/atom for the atoms of the quantum part. The only structural rearrangements are concentrated on the substrate, which moves slightly towards the equatorial oxygen. The transition state is characterized by a distance of ~1.25 Å between the abstracted hydrogen and the equatorial oxygen for both the mimic and the enzyme. The carbon-oxygen distance of the substrate contracts from ~1.4 Å to ~1.3 Å and the angle between the two remaining hydrogens enlarges from 108° to 117°, typical for a ketyl-like intermediate. The leaving hydrogen is in both cases in hydrogen bond contact with the oxygen atom of the substrate. In addition, the hydroxyl proton of the axial tyrosine Tyr495 forms a hydrogen bond with the same donor. Owing to the different orientation of the axial ligand, the corresponding proton in the mimic maintains instead the intramolecular hydrogen bond to N1 already present in **B**.

The activation barrier we calculate for the natural system is 16 kcal/mol, in close agreement with a value of 14 kcal/mol estimated from the experimental turnover rate of 800 s^{-1} [22]. The corresponding value for the synthetic system, on the other hand, is distinctly higher at 21 kcal/mol, consistent with its much lower catalytic activity (turnover numbers for aromatic substrates are ~0.02 s^{-1} [40]).

As in the case of $\mathbf{A}^{ox}$, we performed a number of computer experiments in order to pinpoint the crucial factors responsible for the lowering of the barrier in the natural system. As a first option, we probed the effect of the surrounding protein by fixing the geometry of the quantum part in one defined configuration and relaxing the wavefunction with the external field turned off. A slightly enhanced value of 17 kcal/mol obtained in this way indicates that the external field of the protein has only a small stabilizing effect on the barrier and that therefore the main differences between the mimic and the natural systems are caused by local geometric or electronic properties. In an similar way, we tested the effect of the water molecules present in the active site and found that they have no stabilizing effect on the barrier. The activation barrier without additional solvent molecules turns out to be even slightly smaller (14 kcal/mol).

Electronic structure

In search of a rationale for the difference in the activation energies between the mimetic and the natural systems, we analyzed their electronic structures. The main electronic features of the transition state are again remarkably similar: in both systems the second unpaired electron, which is localized on the equatorial oxygen ligand in **B**, is in **C** mainly located on the substrate itself (Fig. 8, upper half). This finding offers a first explanation for the experimental fact that GOase is several orders of magnitude more efficient in the conversion of aromatic as compared to aliphatic substrates and that the synthetic system only converts aromatic but not aliphatic alcohols [40]. The strong concentration of the unpaired spin density on the alcohol substrate in the transition state suggests that the experimentally observed differences in reactivity are caused by the fact that aromatic substrates form more stable radical intermediates due to the additional delocalization of the unpaired electron density. A closer inspection shows that for **C** the unpaired spin density on the substrate is smaller in the natural system (0.6e) (Table 4) than in its mimic (0.7e). In fact, in GOase the unpaired β-spin density is delocalized to some extent over the equatorial tyrosine and the covalent sulfur link, whereas at the same contour level no net spin population can be found on the equatorial ligand of the mimetic system (Fig. 8, lower half). For the synthetic analog the integrated unpaired spin density is lower than 0.01e for any atom of the equatorial ligand system, while corresponding values in GOase range typically from 0.01 to 0.02e per atom. The total unpaired electron density of the equatorial ligand is roughly twice as large in the natural compound, which provides a first possible rationale of the discrepancy in barrier height. This difference in spin population of the equatorial ligand is also not affected by the external field. At a fixed geometry the only effect of the protein field is to lower the unpaired spin density on the copper ion by 0.2e. Thus, the sulfur-containing ligand has almost no radical character in the biomimetic, in contrast to the natural, system. This agrees with the experimental observation that the covalent sulfur link plays an important role for the catalytic function of GOase [17], whereas sulfur substituents have only a small or no effect for the synthetic compounds [33, 40]. The subtle electronic difference between the natural and the synthetic systems is caused by a particular variance in the geometric properties. All the essential orbitals hosting the unpaired β-spin density are coplanar with the $d_{x^2-y^2}$ orbital at the copper in both the natural and the mimetic systems. However, owing to the perpendicular orientation of Tyr272 the p_z orbitals of the aromatic system and the covalently linked sulfur atom can easily overlap with these orbitals on the former, while owing to the different orientation of the equatorial ligand they are orthogonal in the latter. From Fig. 8 it is apparent that the antiferromagnetic

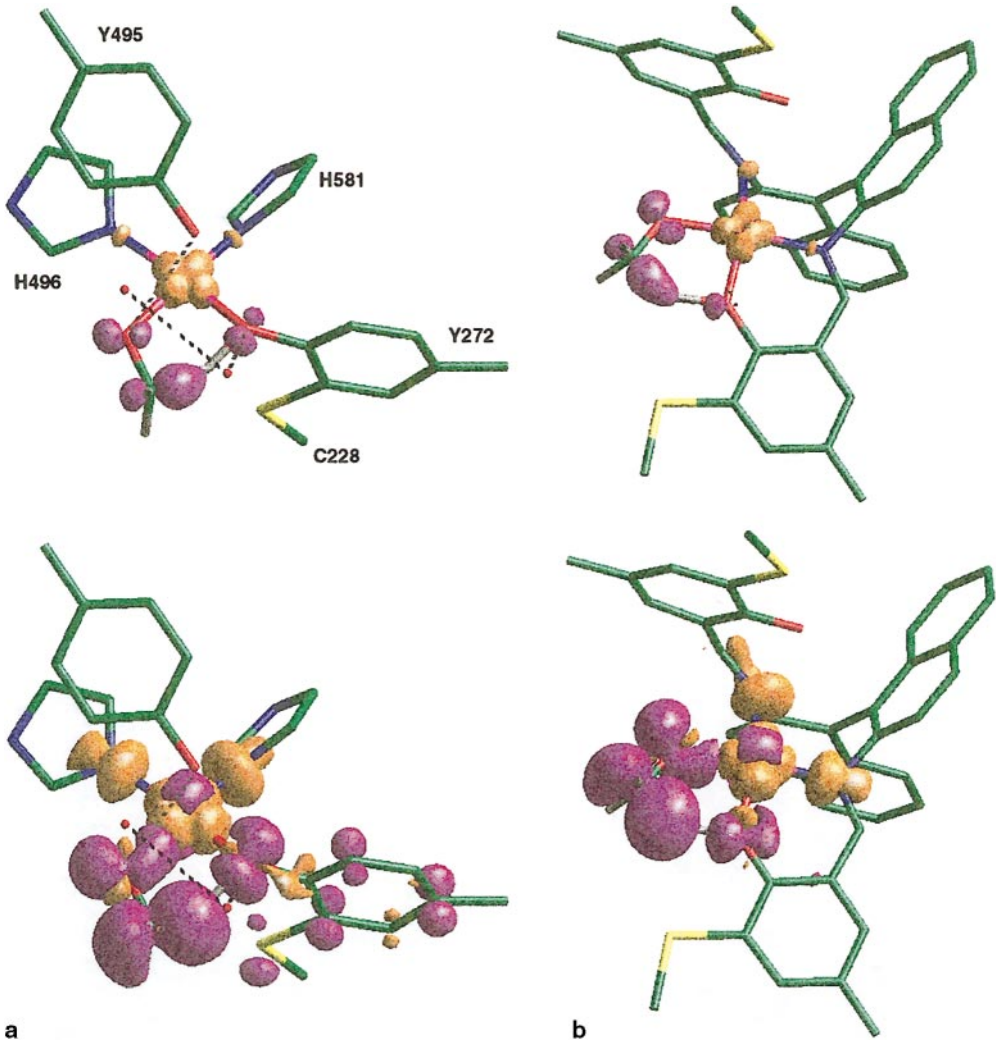

Fig. 8 Comparison of the unpaired electron density distribution in the transition state for hydrogen abstraction (**C**) for **a** GOase and **b** the biomimetic compound. Contours are drawn at two different levels: 0.0015e/au^3 (*upper half*) and 0.001e/au^3 (*lower half*). *Orange* and *magenta* refer to α- and β-spin densities, respectively

nature is still maintained in the transition state, indicating that the electron transfer from the ketyl species to the copper ion occurs *after* the hydrogen abstraction. However, we find that in the synthetic compound the electron transfer happens spontaneously (or with only a very small barrier) upon relaxation to the product **D**, suggesting that hydrogen abstraction and electron transfer take place quasi-simultaneously.

Product of the hydrogen abstraction step **D**

For the natural and the mimetic systems we obtain a closed-shell Cu(I) compound with no significant unpaired spin distribution as a product of the abstraction step. Characteristic structural properties of the products are listed in Table 3. The active site structure of the enzyme changes only slightly in going from the transition state **C** to the product **D**. The main changes affect the direct reaction partners themselves. The copper-oxygen distance to the equatorial tyrosine elongates upon hydrogenation (2.31 Å) and the substrate rotates slightly away from Tyr272 (Fig. 9a). With a carbon-oxygen double bond ($d_{C\text{-}O} = 1.23$ Å) and an HCH angle of almost 120° ($\angle$ HCH = 117°), its structure is now fully characteristic of an aldehydic species. The long copper-oxygen distance ($d_{Cu\text{-}O} = 2.66$ Å) indicates that the aldehyde product is only weakly coordinated and can easily be released and replaced by molecular oxygen, the substrate of the second half-reaction. Apart from the longer Cu-O distance to the equatorial tyrosine, the copper coordination bonds are reminiscent of the resting state of GOase. Even though some large deviations between the Cu(I) product in **D** and the Cu(II) complex in **A** are apparent for the coordination angles, the relative structural likeness suggests that GOase can complete the entire catalytic cycle with only minor geometric rearrangements.

This is in contrast to the mimetic system, for which a substantial geometric rearrangement in the product configuration takes place. The aldehyde substrate rotates away from the equatorial oxygen ligand until the oxygen of the substrate is oriented in a collinear

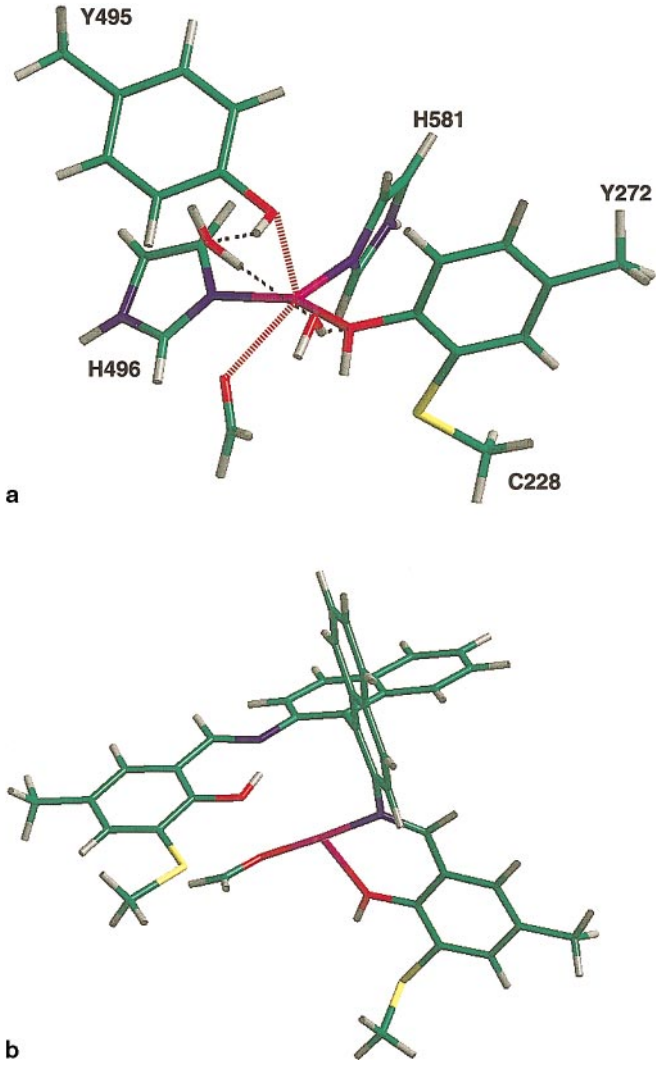

Fig. 9 Structure of the product **D** of the abstraction step for **a** GOase and **b** the biomimetic compound. The long coordination bonds to Tyr495 and the substrate are indicated with *dashed lines*

way with the Cu-N2 axes (Fig. 9b). Simultaneously, the alkyl group on the equatorial thioether changes from a conformation in which the S-C bond is in-plane with the aromatic system to one where it is almost perpendicular (85°). This is a partial reversion of the structural transformation of the alkyl group that we observed earlier upon substrate binding. In addition, the nitrogen atom N1 loses its coordination to the Cu(I) ion. This particular structural change seems to be stabilized by a gain in conjugation. N1 serves as a link atom between the axial oxygen-containing aromatic ring and the adjacent biannular system. Already in **B** and **C** the two aromatic systems assumed an almost parallel conformation. However, there the two do not lie in the same plane because the particular position of N1 (coordinated to the copper ion) induces a parallel shift between the two ring systems. In **D**, N1 has moved away from the copper in such a way that the whole extended aromatic system lies now essentially in one single plane. This leaves the Cu(I) ion in an almost linear coordination with two short bonds (1.84 Å and 1.85 Å) to the nitrogen atom N2 and the substrate oxygen and a longer bond (2.38 Å) to the protonated oxygen O2. In contrast to the natural system, the aldehyde substrate is tightly bound, as indicated by the short Cu-O distance of 1.85 Å. This suggests that the release of the substrate is more difficult in the mimetic system. Furthermore, to regain the initial resting state, the rather drastic geometric changes occurring for **D** have to be reversed in the oxidation half-cycle. Owing to the low coordination of the Cu(I) ion, it is conceivable that molecular oxygen binds when the aldehyde is still present, while for GOase a ping-pong mechanism seems more likely.

Summary and conclusions

We have investigated a number of essential forms of the catalytic cycle of GOase in direct comparison with one of its model compounds. The synthetic analog was described entirely at the gradient-corrected density functional level, whereas we adopted an analogous mixed QM/MM approach for the treatment of the enzyme. In this way, mechanistic differences between the natural and the synthetic systems could be monitored directly throughout the catalytic reaction.

We find that the overall features of the mimetic compound are qualitatively remarkably similar to the ones of its natural target. For both systems the semi-reduced resting state $\mathbf{A}^{semi}$ is characterized by an unpaired electron localized in a $d_{x^2-y^2}$ orbital at the Cu(II) center, while the catalytically active species $\mathbf{A}^{ox}$, the protonated intermediate **B**, and the transition state of the hydrogen abstraction step **C** form antiferromagnetically coupled diradical states. In $\mathbf{A}^{ox}$–**C**, one electron remains localized on the Cu(II) ion, whereas the localization of the second electron of opposite spin varies several times throughout the cycle. All variations of the β-spin distribution from a localization on the *axial* tyrosine Tyr495 in $\mathbf{A}^{ox}$ to the *equatorial* tyrosine Tyr272 in **B** and to a localization on the alcohol substrate in **C** are closely matched by the synthetic active site analog. However, we have also found a number of intrinsic differences between the natural and the synthetic systems that can be summarized as follows:

1. Throughout the catalytic cycle the active site of GOase undergoes only very small geometric changes. The RMS deviations of all the investigated structures **A–D** are smaller than 0.01 Å for all the ~70–80 atoms of the active site quantum region. In the biomimetic system, on the other hand, at least two significant structural rearrangements occur: one upon substrate binding and another in the product formation of the abstraction step.

2. Substrate binding in the mimetic system seems to be hampered by alkyl residues of the thioether groups in *ortho* positions of the equatorial oxygen ligand. Considering the fact that the alcohol substrate is only weakly bound prior to deprotonation, the energy needed to induce a conformational change additionally disfavors the formation of the substrate complex.
3. Adjacent oxygen- and nitrogen-containing aromatic ligands of the biomimetic compound form an angle of 50° in the resting state. However, protonation of the axial ligand and the formation of the product **D** favor the formation of an extended conjugated system in which both ligand systems are essentially coplanar. This energetically favorable competitive configuration leads to large structural changes and induces the formation of a linear NCu(I)O product in which the aldehyde substrate is tightly bound and cannot be released as easily as in the corresponding weakly bound Goase analog.
4. The activation energy for the hydrogen abstraction step is significantly higher in the mimetic compound (21 kcal/mol) than in the natural one (16 kcal/mol). We suggest that this difference is mainly caused by the fact that in GOase the unpaired electron density of the ketyl radical is in part delocalized over the equatorial sulfur-modified tyrosine. Owing to the unfavorable in-plane orientation of the equatorial ring system, this additional stabilization is almost completely absent in the mimetic compound. We have performed a series of computer experiments to evaluate decisive factors involved in the enzymatic catalysis. The protein field outside the quantum region has only a relatively small effect. Most of the crucial properties seem to be determined by the geometric and electronic features of approximately 100 atoms of the active site. Thus, it should indeed be possible to construct small synthetic analogs that can mimic the enzymatic chemistry with high fidelity. This study provides direct mechanistic information that can help in the future design of GOase mimics with increased efficiency or selectivity.

Acknowledgements Calculations were performed on a Cray T3E located at the CINECA Supercomputing Center in Bologna (Italy), a Cray T3E of the Max-Planck Gesellschaft in Garching (Germany), and an IBM-SP of the Competence Center for Computational Chemistry C^4 at the ETH in Zurich (Switzerland). One ofus (P.C.) acknowledges MURST-COFIN for financial support.

References

1. Whittaker J W (1994) In: Sigel H, Sigel A (eds) Metals ions in biological systems, vol 30. Dekker, New York, pp 315–360
2. Whittaker JW, Whittaker MM (1998) Pure Appl Chem 70:903–910
3. Klinman JP (1996) Chem Rev 96:2541–2561
4. Whittaker MM, De Vito VL, Asher SA, Whittaker JW (1989) J Biol Chem 264:7104–7106
5. Whittaker MM, Whittaker JW (1990) J Biol Chem 265:9610–9613
6. Whittaker MM, Chuang YY, Whittaker JW (1993) J Am Chem Soc 115:10029–10035
7. Gerfen GJ, Bellew BI, Griffin RG, Singel DJ, Ekberg CA, Whittaker JW (1996) J Phys Chem 100:16739–16748
8. Whittaker MM, Kersten PJ, Nakamura N, Saunders-Loehr J, Schweizer ES, Whittaker JW (1996) J Biol Chem 271:681–687
9. Licht S, Gerfen GJ, Stubbe J (1996) Science 271:477–481
10. Goodin DB, McRee DE (1993) Biochemistry 32:3313–3324
11. Tsai A, Kulmacz RJ, Palmer G (1995) J Biol Chem 270:10503–10508
12. Hoganson CW, Lydajis-Simantiris N, Tang X-S, Tommos C, Warncke K, Babcock GT, Diner BA, McCracken J, Styring S (1995) Photosynth Res 46:177–184
13. Harkins TT, Grissom CB (1994) Science 263:958–960
14. Zhao Y, Abend A, Kunz M, Such P, Retey J (1994) Eur J Biochem 225:891–896
15. Ito N, Phillips SEV, Stevens C, Ogel ZB, McPherson MJ, Keen JN, Yadav KDS, Knowles PF (1991) Nature 350:87–90
16. Ito N, Phillips SEV, Yadav KDS, Knowles PF (1994) J Mol Biol 238:794–814
17. Baron A, Stevens C, Wilmot C, Seneviratne KD, Blakeley V, Dooley DM, Phillips SEV, Knowles PF, McPherson MJ (1994) J Biol Chem 269:25095–25105
18. Hamilton GA, Adolf PK, de Jersey J, DuBois GC, Dyrkacz GR, Libby RD (1978) J Am Chem Soc 100:1899–1912
19. Borman CD, Saysell CG, Sykes AG (1997) JBIC 2:480–487
20. Whittaker MM, Ballou DP, Whittaker JW (1998) Biochemistry 37:8426–8436
21. Whittaker MM, Whittaker JW (1988) J Biol Chem 263:6074–6080
22. Wachter RM, Branchaud BP (1998) Biochim Biophys Acta 1384:43–54
23. Whittaker MM, Whittaker JW (1993) Biophys J 64:762–772
24. Reynolds MP, Baron AJ, Wilmot CM, Phillips SEV, Knowles PF, McPherson MJ (1995) Biochem Soc Trans 23:510S
25. Borman CD, Saysell CG, Wright C, Sykes AG (1998) Pure Appl Chem 70:897–902
26. Branchaud BP, Montague-Smith MP, Kosman DJ, McLaren FR (1993) J Am Chem Soc 115:798–800
27. Wachter RM, Montague-Smith MP, Branchaud BP (1997) J Am Chem Soc 119:7743–7749
28. Johnson JM, Halsall HB, Heineman WR (1982) Anal Chem 54:1394–1399
29. Adams H, Bailey NA, Campell IK, Fenton DE, He QY (1996) J Chem Soc Dalton Trans 2233–2237
30. Wang Y, Stack TDP (1996) J Am Chem Soc 118:13097–13098
31. Halfen JA, Young VG Jr, Tolman WB (1996) Angew Chem Int Ed Engl 35:1687–1690
32. Whittaker MM, Duncan WR, Whittaker JW (1996) Inorg Chem 35:382–386
33. Halfen JA, Jazdzewski BA, Mahapatra S, Berreau LM, Wilkinson EC, Que L Jr, Tolman WB (1997) J Am Chem Soc 119:8217–8227
34. Sokolowski A, Leutbecher H, Weyermüller T, Schnepf R, Bothe E, Bill E, Hildebrandt P, Wieghardt K (1997) JBIC 2:444–453

35. Fontecave M, Pierre JL (1998) Coord Chem Rev 170:125–140
36. Vaidyanathan M, Viswanathan R, Palaniandavar M, Balasubramanian T, Prabhaharan P, Muthiah TP (1998) Inorg Chem 37:6418–6427
37. Ito S, Nishino S, Itoh H, Ohba S, Nishida Y (1998) Polyhedron 17:1637–1642
38. Ruf M, Peripont CG (1998) Angew Chem Int Ed Engl 37:1736–1739
39. Halcrow MA, Chia LML, Liu X, McInnes EJL, Yellowlees LJ, Mabbs FE, Davies JE (1998) J Chem Soc Chem Commun 2465–2466
40. Wang Y, Dubois JL, Hedman B, Hodgson KO, Stack TDP (1998) Science 278:537–540
41. Chaudhuri P, Hess M, Flörke U, Wieghardt K (1998) Angew Chem Int Ed Engl 37:2217–2220
42. Chaudhuri P, Hess M, Weyermüller T, Wieghardt K (1999) Angew Chem Int Ed Engl 38:1095–1098
43. Rothlisberger U, Carloni P (1999) Int J Quantum Chem 73:209–218
44. Gao J, Thompson M A (eds) (1998) Combined quantum mechanical and molecular mechanical methods. (ACS symposium series 712) American Chemical Society, Washington
45. Eichinger M, Tavan P, Hutter J, Parrinello M (1999) J Chem Phys 110:10452–10467
46. Car R, Parrinello M (1985) Phys Rev Lett 55:2471–2474
47. Hohenberg P, Kohn W (1964) Phys Rev B 136:864
48. Kohn W, Sham LJ (1965) Phys Rev A 140:1133
49. Hutter J, Ballone P, Bernasconi M, Focher P, Fois E, Goedecker S, Parrinello M, Tuckerman M (1995/96) CPMD. MPI für Festkörperforschung, Stuttgart, and IBM Research Laboratory, Zurich
50. Troullier N, Martins JL (1991) Phys Rev B 43:8861–8869
51. Becke AD (1988) Phys Rev A 38:3098–3100
52. Lee C, Yang W, Parr RG (1988) Phys Rev B 37:785–789
53. Hockney RW (1970) Methods Comput Phys 9:135–211
54. Marx D, Fois E, Parrinello M (1996) Int J Quantum Chem 57:655–662
55. CERIUS2 (Version 3.8) Molecular Simulation, Inc. San Diego (1998)
56. Mayo SL, Olafson BD, Goddard WA (1990) J Phys Chem 94:8897–8909
57. Rappe AK, Goddard WA (1991) J Phys Chem 95:3358–3363
58. Eichinger M, Grubmüller H, Heller H (1995) EGO VIII, release 2.0. Ludwig-Maximilian-Universität, Munich
59. Brooks BR, Bruccoleri RE, Olafgson BD, States DJ, Swaminathan S, Karplus M (1983) J Comput Chem 4:187–217
60. Eichinger M, Grubmüller H, Heller H, Tavan P (1997) J Comput Chem 18:1729–1749
61. Brünger AT (1990) X-PLOR, version 2.1. Yale University, New Haven
62. Ryckaert JP, Ciccotti G, Berendsen HJC (1977) J Comput Phys 23:327–341
63. Brooks CL III, Karplus M, Pettitt BM (1988) Adv Chem Phys 71:1–259
64. Knowles PF, Brown RD III, Koenig SH, Wang S, Scott RA, McGuirl MA, Brown DE, Dolley DM (1995) Inorg Chem 34:3895–3902